EES Batteries

Check for updates

A fluorine-free electrolyte for calcium metal batteries

Andrii Kachmar, †[a] Robert Markowski, †[a] Taniya Purkait,[a] Darsi Rambabu,[a] Petru Apostol,[a] Da Tie,[a] Roy Heyns,[b] Jan Fransaer,[c] Koen Binnemans,[b] Alexandre Ponrouch[d,e] and Alexandru Vlad *[a,f]

Calcium metal batteries (CMBs) have emerged as a promising alternative to lithium(Li)-based technologies due to calcium's (Ca) low reduction potential, high volumetric capacity, and abundance. However, challenges such as poor Ca^{2+} transport across passivation layers and limited electrolyte compatibility hinder practical implementation. Here, we report a fluorine-free electrolyte formulation based on calcium bis(methanesulfonimide) ($Ca(MSI)_2$) in dimethylacetamide (DMAc). This system offers a safer, more sustainable, and environmentally benign alternative to conventional fluorinated electrolytes. Comparative physicochemical and electrochemical evaluations with the benchmark $Ca(TFSI)_2$/DMAc electrolyte reveal that $Ca(MSI)_2$ enables stable calcium plating/stripping over 1600 hours with lower overpotential and improved rate performance. In fact, spectroscopic analyses confirm the formation of a more uniform, fluorine-free interphase that supports better Ca^{2+} transport throughout the passivation layer. These findings highlight the potential of fluorine-free salts for enabling reversible room temperature calcium metal cycling and advance the development of safer, high-performance multivalent batteries.

Broader context

Developing sustainable electrolytes is central to advancing next-generation electrochemical energy storage (EES) technologies. Beyond lithium-ion systems, multivalent batteries such as calcium and magnesium promise higher volumetric capacity, elemental abundance, and safer operation. Yet, their progress is limited by unstable passivation layers and the reliance on fluorinated salts, which often generate resistive interphases and environmentally persistent byproducts. In this study, we introduce a fluorine-free calcium electrolyte based on calcium bis(methanesulfonimide) ($Ca(MSI)_2$). Demonstrated here in calcium metal batteries as a model multivalent system, the electrolyte enables highly reversible Ca plating and stripping at room temperature with improved stability and lower overpotentials compared to fluorinated analogues. The absence of fluorine avoids CaF_2-rich interphases and instead promotes a more uniform, ion-conductive passivation layer. By coupling sustainability with interfacial functionality, this work highlights design rules for halogen-free electrolytes, offering pathways applicable across emerging multivalent and beyond-lithium battery chemistries.

Multivalent batteries based on Mg^{2+} and Ca^{2+} are emerging as promising alternatives to lithium-ion batteries (LIBs), owing to their elemental abundance, lower dendrite risk, and potential for multi-electron redox processes.[1–5] Batteries based on calcium metal anode are particularly attractive, offering the lowest redox potential (−2.87 V *vs.* SHE) and a high volumetric capacity of 2073 mAh cm^{-3} – comparable to that of lithium metal.[6] In addition, the lower charge density of Ca^{2+} compared to Mg^{2+} resulting in lower coulombic interactions potentially favoring power performance.[7] Despite these advantages, calcium battery development is challenged by interfacial limitations – especially the formation of passivating layers in most electrolytes that hinder Ca^{2+} transport. Such passivation layer formation being favored by calcium standard redox potential being 500 mV lower the magnesium's one.

Reversible calcium plating and stripping require the optimization of two key interfacial processes: Ca^{2+} transport through the passivation layer and its desolvation at the electrolyte/pas-

[a] Institute of Condensed Matter and Nanosciences, Molecular Chemistry, Materials and Catalysis, Université catholique de Louvain, Louvain-la-Neuve B-1348, Belgium. E-mail: alexandru.vlad@uclouvain.be

[b] Department of Chemistry, SOLVOMET R&I Centre, KULeuven, Celestijnenlaan 200F, Box 2404, 3001 Heverlee, Belgium

[c] Department of Materials Engineering, KULeuven, 3001 Leuven, Belgium

[d] Institut de Ciència de Materials de Barcelona, ICMAB-CSIC, Campus UAB, Bellaterra, Catalonia 08193, Spain

[e] ALISTORE-European Research Institute, CNRS FR 3104, Hub de l'Energie, Rue Baudelocque, Amiens 80039, France

[f] WEL Research Institute, Avenue Pasteur, 6, 1300 Wavre, Belgium

† These authors contributed equally to this work.

sivation interface. A major breakthrough came in 2016, when Ponrouch et al.[8] demonstrated reversible calcium deposition using $Ca(BF_4)_2$ in an EC : PC solvent blend at elevated temperatures (70–100 °C). This system formed a mixed organic–inorganic passivation layer that allowed Ca^{2+} diffusion to some extent, with boron cross-linked polymeric matrices present in the passivation layer potentially playing an important role allowing for Ca plating.[9,10] The composition of passivation layers can significantly affect Ca^{2+} mobility. Density functional theory (DFT) calculations indicate that the migration barriers vary considerably among different interphase components: CaF_2 (~2046 meV) and $CaCO_3$ (~1436 meV) are highly resistive, CaO is moderately conductive (~997 meV), while CaH_2 exhibits the lowest barrier (~541 meV), consistent with its favorable ion transport characteristics.[9,11,12] Room-temperature calcium plating was later realized using $Ca(BH_4)_2$-based electrolytes, which generate a CaH_2-rich SEI that enabled sufficient Ca^{2+} transport.[13–16] However, their limited anodic stability and high reactivity restrict compatibility with high-voltage cathodes and non-ether solvents.[10] To address this, more anodically stable salts – such as $Ca[B(hfip)_4]_2$ and $Ca[Al(hfip)_4]_2$ – were developed, enabling operation above 3 V.[11,17–20] However, these salts are synthetically complex, expensive, and sensitive to impurities.

As an alternative strategy, Hou et al.[21] introduced a high-donor solvent, dimethylacetamide (DMAc), combined with Ca(TFSI)₂. This system facilitated reversible Ca cycling at low over-potentials by forming an organic-rich SEI. While inorganic components may still be needed for long-term stability,[22] the DMAc-based formulation favored the formation of solvent-separated ion pairs (SSIPs), which reduced polarization and minimized the need for complex electrolyte engineering. Despite initial success, long-term cycling with $Ca(TFSI)_2$ revealed increasing polarization, attributed to TFSI⁻ decomposition and CaF_2 accumulation at the interface.[9,21] Although TFSI⁻ is bulky and charge-delocalized, it tends to form contact ion pairs (CIPs) above 0.5 M – even in high donor number solvents – leading to anion reduction and a brittle, ion-insulating passi-

vation layer.[23,24] In response to these limitations and growing safety and environmental concerns over halogenated compounds, we synthesized $Ca(MSI)_2$, a fluorine-free analogue of $Ca(TFSI)_2$, and paired it with DMAc.

This new formulation demonstrated improved performance, achieving lower polarization (0.82 V vs. 0.95 V with TFSI) and stable cycling for over 1600 h at 0.02 mA cm⁻². Characterization showed that $Ca(MSI)_2$ produces a thinner, more uniform SEI with reduced interfacial decomposition. Differences in anion geometry and coordination strength influence CIP formation and desolvation dynamics, shaping the resulting SEI structure and ion transport properties. The enhanced stability of $Ca(MSI)_2$ highlights that improved ionic mobility and SEI uniformity can reduce the need for inorganic interphase engineering.[9] Furthermore, its fluorine-free nature not only prevents CaF_2 formation but also aligns with sustainability goals by avoiding the energy-intensive synthesis of C–F bonds. Recent studies (He et al.[25,26]) have underscored the importance of developing fluorine-free calcium electrolytes for improved electrochemical reversibility, reduced environmental impact, and safer large-scale battery deployment.

$Ca(MSI)_2$ was synthesized by first preparing the MSI ligand, following the method reported by Zhang et al.,[27] using inexpensive and commercially available reagents, methanesulfonyl chloride and methanesulfonylamine. In contrast to the classic multistep, low-temperature synthesis of bis(trifluoromethylsulfonyl)imide,[28] which involves electrochemical fluorination in anhydrous HF and produces toxic by-products, MSI can be synthesized safely and cost-effectively from readily available non-fluorinated reagents under mild conditions. The full experimental procedure is described in detail in the SI, and cost calculations are provided in Table S1. Calcium salt of MSI was then prepared via a solid-state mechano-thermal approach. Specifically, MSI and calcium acetate $(Ca(OAc)_2)$ were mixed and subsequently heated at 200 °C under vacuum (Scheme 1B). This annealing temperature was guided by thermogravimetric analysis (TGA), which showed that the MSI ligand is thermally stable under the applied synthesis con-
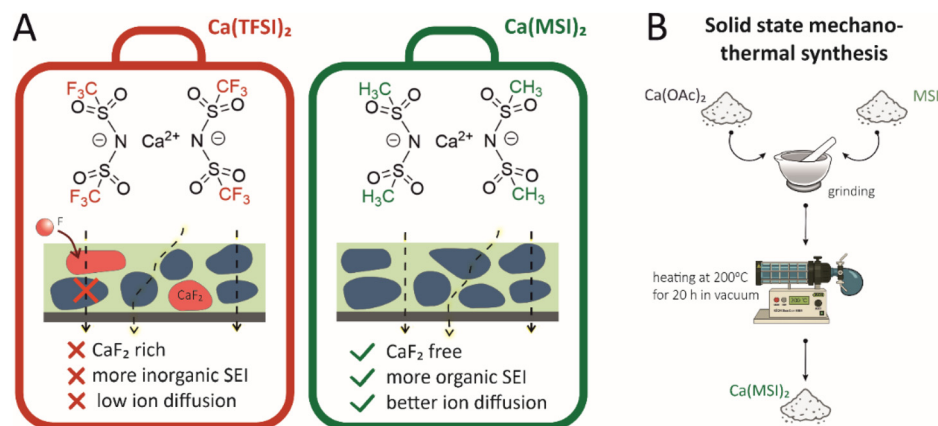
Scheme 1 (A) Interfacial behaviour and molecular structures of Ca(TFSI)₂ and Ca(MSI)₂ electrolytes. (B) Synthesis of Ca(MSI)₂ via solid-state reaction by calcium acetate (Ca(OAc)₂), and dimesylamine (MSI), followed by grinding and heating.

ditions. Furthermore, the resulting $Ca(MSI)_2$ exhibits excellent thermal stability, remaining stable up to 349 °C as confirmed by TGA (Fig. S1).

The synthesized $Ca(MSI)_2$ salt was characterized by Fourier transform infrared spectroscopy (FTIR), elemental analysis, nuclear magnetic resonance (NMR) spectroscopy, and powder X-ray diffraction (PXRD), (Fig. 1). FTIR spectroscopy corroborates the formation of $Ca(MSI)_2$ (Fig. 1A). The broad N–H stretching band observed between 3050–3250 cm^{-1} in the free ligand is absent in the salt, consistent with full ligand deprotonation. Shifts in the characteristic S=O stretching bands within the 1300–1100 cm^{-1} region upon salt formation indicate coordination between sulfonyl groups and the calcium cation. Complementary CHNS elemental analysis and ICP-OES measurements (Table S2) further confirm the successful synthesis and purity of the $Ca(MSI)_2$ salt. NMR spectra provide further confirmation of the formation and purity of $Ca(MSI)_2$ (Fig. 1B). In the ^1H NMR spectrum of the pristine MSI ligand, the main singlet at ~3.0 ppm corresponds to the six protons from two methyl groups. Upon salt formation, this signal shifts downfield to ~2.7 ppm, reflecting changes in the electronic environment. The loss of the N–H proton resonance at 10.1 ppm (inset) verifies full deprotonation of the MSI ligand and consequent salt formation. No signals attributable to calcium acetate or uncoordinated MSI were observed, confirming the compound's purity. The PXRD pattern of $Ca(MSI)_2$ displays a distinct set of diffraction peaks compared to those of the free MSI ligand and commercial $Ca(OAc)_2$, confirming the formation of a new crystalline phase (Fig. 1C). This structural change also evidences the successful synthesis of a well-defined calcium salt. Moreover, comparison with the XRD pattern of $Ca(TFSI)_2$ (Fig. S2) reveals a shift of diffraction peaks in $Ca(MSI)_2$ toward higher 2θ values, indicating reduced lattice spacings. This shift is consistent with the substitution of the bulkier fluorinated TFSI$^-$ anion by the smaller hydrogen-containing MSI$^-$ anion, resulting in a more compact crystal structure.

We assessed the compatibility of the synthesized Ca salt with various solvents *via* a solubility study. First, different Ca salts were dissolved at 0.1 M in multiple solvents to gauge baseline solubility. Then, $Ca(MSI)_2$ was dissolved to saturation to find its maximum solubility (Fig. 2A). Red bars indicate incomplete dissolution at 0.1 M, green bars – full dissolution. Limited dissociation stems from strong electrostatic interactions between Ca^{2+} and nitrogen-centered MSI$^-$. DMF, DMSO, and DMAc fully dissolved $Ca(MSI)_2$, with DMF and DMSO reaching ~1 mol L^{-1}. Solubility correlated with solvent donor number (DN) and dielectric constant; DMF, DMSO, and
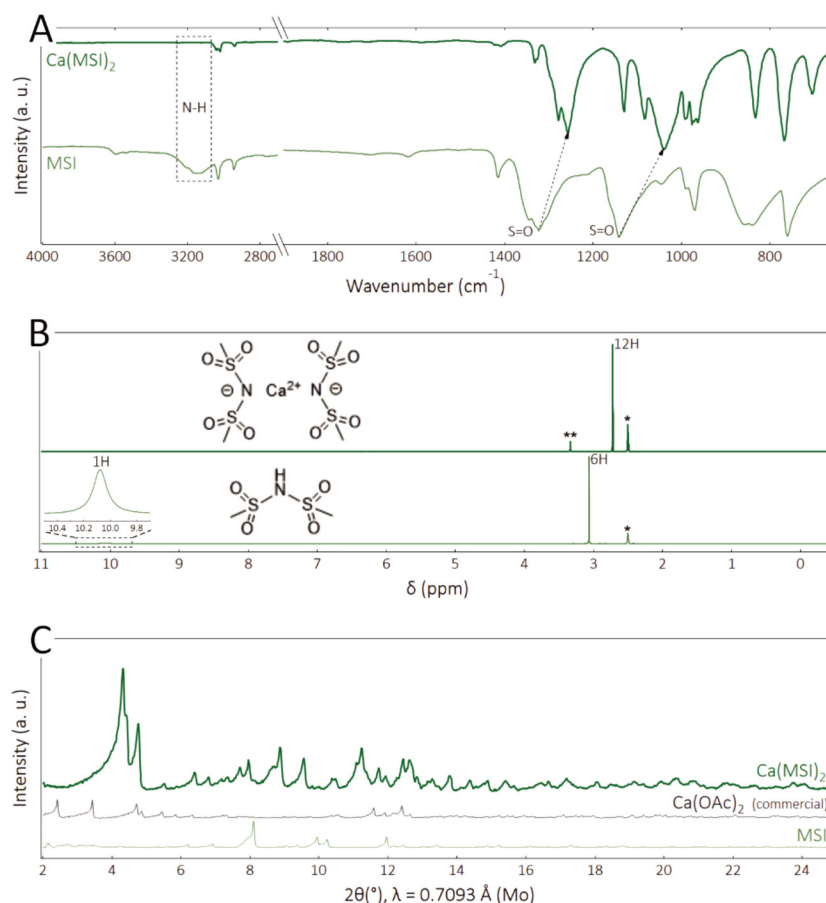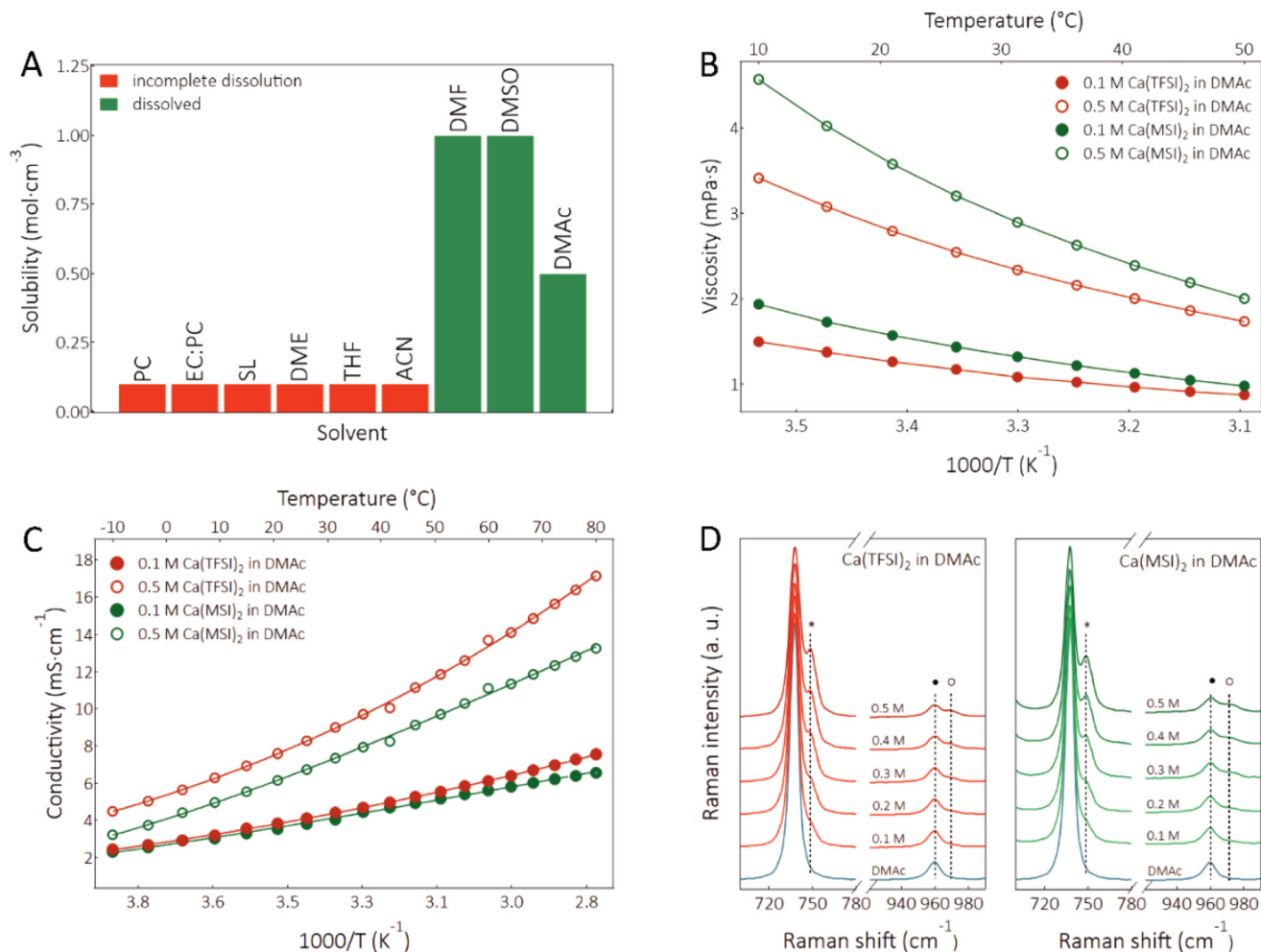

Fig. 1 (A) Infrared spectra of $Ca(MSI)_2$ and MSI, (B) NMR spectra of MSI (*DMSO-d$_6$, **water), (C) The PXRD spectra of $Ca(MSI)_2$, $Ca(OAc)_2$, and MSI.

Fig. 2 (A) Solubility study: solvent effectiveness comparison of Ca(MSI)₂ electrolytes. (B) Viscosity (C), conductivity (solid lines represent the Vogel–Tammann–Fulcher (VTF) fits, see Table S4 for fitting parameters) (D) Raman spectra of Ca(TFSI)₂ and Ca(MSI)₂ in DMAc at different salt concentrations. Filled circle (●) denotes free solvent, while open circle (○) denotes Ca²⁺-coordinated solvent. * – the band assigned to cation–anion contact ion pairs appears in all cases at 748 cm⁻¹.

DMAc have high DN (≥ 26), acting as strong Lewis bases stabilizing Ca²⁺ (Table S3). Low-DN solvents – acetonitrile, propylene carbonate, sulfolane, and ethers – failed to dissolve Ca(MSI)₂, highlighting the critical role of solvent coordination. The detailed experimental conditions and solvation behavior are presented in Fig. S4.

For physicochemical characterization, we focused on DMAc-based electrolytes, shown later to yield the best electrochemical performance. To understand the anion's role, we compared Ca(MSI)₂ and Ca(TFSI)₂, investigating how replacing fluorine with hydrogen affects properties. Viscosity measurements (Fig. 2B) showed the expected increase at lower temperatures. At both concentrations, Ca(MSI)₂ solutions exhibited consistently higher viscosities than Ca(TFSI)₂, suggesting stronger ion-solvent and ion-ion interactions associated with the MSI⁻ anion, despite its lower molecular weight. In both electrolytes, viscosity increased with salt concentration, reflecting enhanced ion pairing and reduced solvent mobility.

Ionic conductivity measurements (Fig. 2D and Table S3, Fig. S5) showed conductivity increasing with concentration for both salts. Ca(TFSI)₂ consistently outperformed Ca(MSI)₂: at 20 °C, 0.1 M solutions had conductivities of 4.13 mS cm⁻¹ (TFSI) vs. 3.80 mS cm⁻¹ (MSI), rising to 8.28 and 6.74 mS cm⁻¹ at 0.5 M. This difference is attributed to the bulkier, more charge-delocalized TFSI⁻, which promotes greater ion dissociation and mobility. The smaller MSI⁻ likely forms tighter ion pairs with Ca²⁺, reducing free charge carriers and, along with higher viscosity, lowering conductivity. Despite this, the differences are small, suggesting both support effective ion transport under these conditions.

Raman spectral analysis was conducted to gain deeper insight into ion pairing and solvation structures in both Ca salt systems. As shown in Fig. 2D, the characteristic vibrational modes of the free TFSI⁻ and MSI⁻ anions (740 cm⁻¹ according to Forero-Saboya et al.²⁹) overlap with the strong solvent band of DMAc at 739 cm⁻¹, which complicates direct observation of

uncoordinated anions. Nevertheless, ion pairing is clearly evidenced by the emergence of a distinct band at 748 cm^{-1}. In the case of the Ca(TFSI)$_2$ system, this band is assigned to the formation of [CaTFSI]$^+$ contact ion pairs. A similar spectral evolution is observed in the Ca(MSI)$_2$ system, where the intensity of the [CaMSI]$^+$ feature increases with salt concentration (Fig. S7). This indicates enhanced interactions between Ca^{2+} and the MSI$^-$ anion and confirms the formation of contact ion pairs in both systems.

In parallel, another key observation is the evolution of the DMAc solvent peak at 960 cm^{-1}, which corresponds to free, uncoordinated solvent molecules. As salt concentration increases, the intensity of this peak gradually decreases, accompanied by the emergence of a new band corresponding to DMAc coordinated to Ca^{2+} ions. This shift is consistently observed for both salts and indicates that Ca^{2+} increasingly interacts with the solvent molecules at higher concentrations, leading to more pronounced cation-solvent coordination. Taken together, these spectral characteristics illustrate the gradual evolution of solvation structures and the growing extent of ion association as concentration rises.

The formation and nature of contact ion pairs are closely linked to the properties of the anions. As previously reported by Forero-Saboya et al.,[9] the TFSI$^-$ anion, due to its large size, conformational flexibility, and high degree of charge delocalization, tends to form fewer contact ion pairs compared to more localized anions like BF$_4^-$, which are readily incorporated into the first solvation shell. In our study, the MSI$^-$ anion appears to behave similarly to TFSI$^-$, despite its smaller size and relatively higher charge density. The gradual increase of the [CaMSI]$^+$ Raman signal with concentration, without strong evidence for tight ion clustering or sharp decreases in conductivity, suggests that MSI$^-$ also acts as a relatively weakly coordinating anion.

Raman analysis (Fig. S7) indicates somewhat stronger contact ion pair (CIP) features in Ca(TFSI)$_2$ compared to Ca(MSI)$_2$, which could at first seem to contradict the higher conductivity observed for the TFSI$^-$-based electrolyte. However, this difference can be rationalized by considering both the nature of ion association and the overall mobility of ionic species. Raman spectroscopy probes static (or time-averaged) local coordination, not ion-pair lifetime. Conductivity, however, depends on the dynamic mobility and exchange rate of charged species. So, even if Raman shows more 'CIP-like' spectral features, if those pairs rapidly dissociate or exchange partners, they can still contribute to ionic transport almost as efficiently as free ions.[30–32]

While Ca(TFSI)$_2$ exhibits a higher fraction of CIPs, these ion pairs are less strongly bound and more dynamically dissociating than those formed in Ca(MSI)$_2$. The TFSI$^-$ anion is significantly larger and more charge-delocalized, which reduces coulombic interaction strength and facilitates transient ion dissociation. Consequently, even though the instantaneous CIP population is higher, the lifetime of these associations is shorter, allowing a larger number of charge carriers to contribute to ionic transport. In contrast, the smaller and more localized MSI$^-$ anion forms tighter ion pairs and aggregates with Ca^{2+}, which restricts ion mobility and decreases the effective number of free charge carriers. Therefore, the greater ionic conductivity of Ca(TFSI)$_2$ arises not from a lower degree of ion pairing, but from the higher mobility and weaker binding energy of the associated species, leading to more efficient dynamic ion transport.

In summary, the Raman data reflect the equilibrium ion-association structure, whereas the conductivity measurements capture the dynamic charge-transport behavior. The two observations are consistent when considering that the TFSI$^-$-based electrolyte supports faster ion-pair exchange and higher ion mobility, yielding the observed increase in conductivity. Taken together, Raman analysis reinforces the idea that the substitution of fluorine with hydrogen in the anion structure (from TFSI$^-$ to MSI$^-$) does not drastically alter the fundamental coordination chemistry, but rather offers a fluorine-free alternative with similar physicochemical behavior.

Building on these insights into the comparable coordination environments provided by TFSI$^-$ and MSI$^-$, we next explored how the choice of solvent influences the electrochemical performance of Ca(MSI)$_2$-based electrolytes. We tested Ca(MSI)$_2$ in DMSO, DMF, and DMAc – selected as the only solvents in which the salt was sufficiently soluble. Among them, the DMAc-based electrolyte delivered the best results, showing superior cycling stability and the lowest overpotential (Fig. S9). This observation is consistent with previous findings by Hou et al.,[21] who attributed DMAc's favorable behavior to its strong solvating power that facilitates the formation of solvent-dominated solvation sheaths, thereby suppressing anion decomposition and promoting the formation of an organic-rich, ion-conductive passivation layer.

Having identified DMAc as the optimal solvent, we subsequently performed a direct comparison of calcium plating/stripping behavior in Ca(TFSI)$_2$- and Ca(MSI)$_2$-based electrolytes to isolate and assess the specific influence of the anion on calcium electrochemistry (Fig. 3). A remarkably stable cycling profile was observed in the Ca(MSI)$_2$-based electrolyte for over more than 800 cycles, starting with an overpotential of 0.82 V that gradually increased to 1.75 V after 1600 hours of continuous operation (Fig. 3A). In contrast, a slightly higher initial overpotential of 0.95 V was measured in case of Ca(TFSI)$_2$ electrolyte. Moreover, a sharp and early rise in overpotential was recorded after only ~200 hours of cycling up to 1.25 V (Fig. 3A). A similar cycling behavior was observed in both salts at a lower concentration of 0.1 M (Fig. S8). While Raman spectroscopy and ionic conductivity measurements confirm similar coordination chemistry for both anions in bulk of the solution, the distinct electrochemical responses clearly points to interfacial processes as being the critical differentiator.[9,33,34] The gradual increase in overpotential with time is most likely due to the continuous growth and thickening of this passivation layer. As it becomes denser, ionic diffusion – particularly of Ca^{2+} ions – through the interphase becomes increasingly restricted, thereby requiring a higher
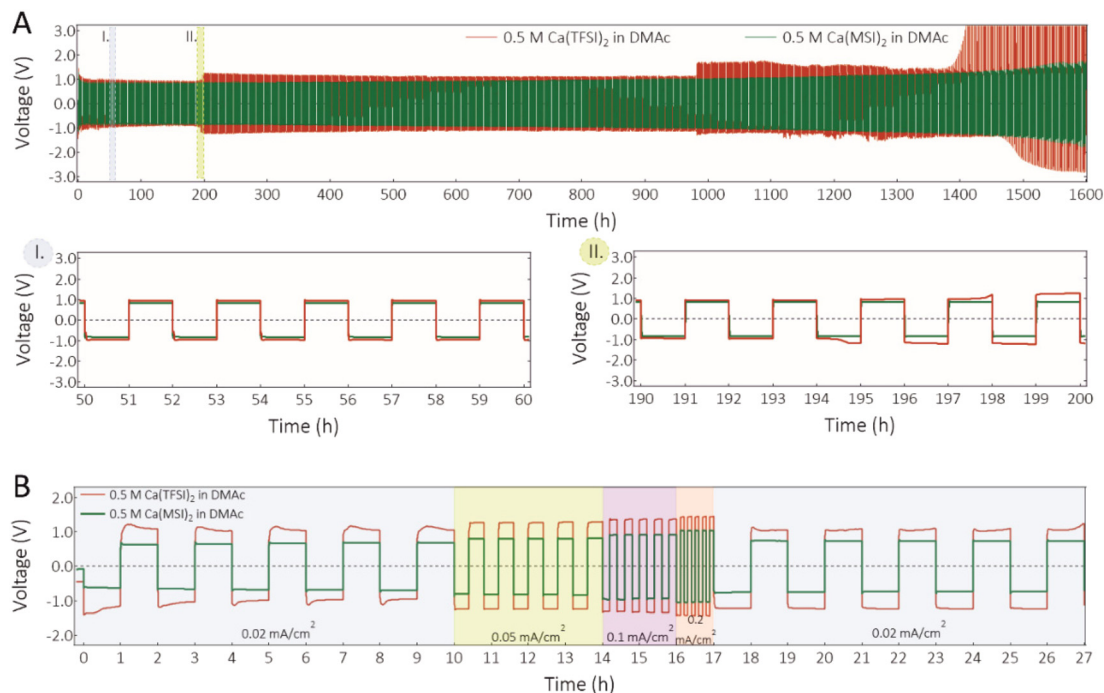
Fig. 3 (A) Cyclic stability at 0.02 mA cm^{-2} and (B) rate capability of Ca/Ca symmetric cells in 0.5 M Ca(MSI)$_2$ and Ca(TFSI)$_2$ in DMAc electrolytes.

driving force (*i.e.*, overpotential) to sustain efficient plating and stripping.[35,36]

To further evaluate kinetic limitations and interphase stability, we carried out electrochemical cycling at varying current densities (0.02, 0.05, 0.1 mA cm^{-2}, and back to 0.02 mA cm^{-2}) (Fig. 3B). Generally stable voltage profiles were maintained in both electrolytes across the range of applied current variations. However, Ca(MSI)$_2$ consistently showed lower and more stable overpotentials than Ca(TFSI)$_2$, indicating a higher electrochemical tolerance of the interface to the rate-induced stress. Upon increasing current density, both systems exhibited rising overpotentials, but Ca(TFSI)$_2$ showed a much sharper increase, along with signs of instability. In contrast, Ca(MSI)$_2$ retained more stable voltage behavior, even under higher current loads. Upon returning to the original low current density, both systems recovered their initial electrochemical performance (Fig. 3B). The differing overpotential trends observed for the Ca(MSI)$_2$ and Ca(TFSI)$_2$ systems are most likely attributed to variations in the composition of the passivation layers formed on the calcium metal surface. These compositional differences, which influence Ca^{2+} transport across the interphase, are discussed in more detail in the following section.

In terms of electrochemical stability, both Ca(TFSI)$_2$ and Ca(MSI)$_2$ electrolytes exhibit stable behavior over the tested cycling range (Fig. S10). The Ca(MSI)$_2$-based electrolyte shows a cathodic stability limit (reduction onset) at approximately −2.88 V, whereas the Ca(TFSI)$_2$-based system becomes reductively unstable at a slightly higher potential of around −2.40 V *vs.* Ca/Ca^{2+}. On the anodic side, Ca(MSI)$_2$ remains stable up to ~4.31 V, while Ca(TFSI)$_2$ exhibits a broader oxidative stability

window, extending to ~4.96 V *vs.* Ca/Ca^{2+}. In both systems, distinct cathodic peaks are observed between −3 V and −1 V *vs.* Ca/Ca^{2+}, likely corresponding to calcium metal plating, electrolyte decomposition, or side reactions occurring at the electrode–electrolyte interface.

To understand how electrolyte chemistry influences calcium plating/stripping, we conducted high-resolution XPS on Ca metal electrodes after 10 cycles in symmetric Ca/Ca cells using Ca(TFSI)$_2$ and Ca(MSI)$_2$ in DMAc at 0.2 mA cm^{-2} (1 h per half-cycle) (Fig. 4A). The F 1s spectra show clear differences: Ca(TFSI)$_2$ exhibits peaks at 687.9 eV and 684.4 eV, assigned to C–F and Ca–F (from CaF$_2$), respectively – products of TFSI$^-$ decomposition.[21] These signals are absent with Ca(MSI)$_2$ (the F 1s signal was only 0.4% of the atomic concentration and originates from trace surface contamination and does not represent an intrinsic component of the Ca(MSI)$_2$ system). In the O 1s region, Ca(TFSI)$_2$ shows a peak at ~532.2 eV by carbonyl, while Ca(MSI)$_2$ features a stronger peak at 529.3 eV (Ca–O bonds), indicating more CaO formation. A peak at 531.1 eV, related to CaCO$_3$, is more intense in the MSI case, alongside a shoulder at 532.9 eV by C–O–C/C–OH.[13,21,37]

The C 1s spectra indicate similar organic species in both electrolytes, but Ca(TFSI)$_2$ uniquely shows –CF$_3$ peaks, confirming incorporation of fluorinated decomposition products.[9] Ca 2p spectra reveal three doublets in Ca(TFSI)$_2$ systems. The main peak at 347.5 eV – CaCO$_3$ is common.[13,38,39] Ca(TFSI)$_2$ also shows a peak at 348.9 eV, which answers CaF$_2$, consistent with F 1s data.[39] A lower-energy peak near 346.9 eV likely corresponds to CaO, and CaH$_2$.[40] Elemental analysis (Fig. 4B and S11) shows high fluorine/sulfur content for Ca(TFSI)$_2$,
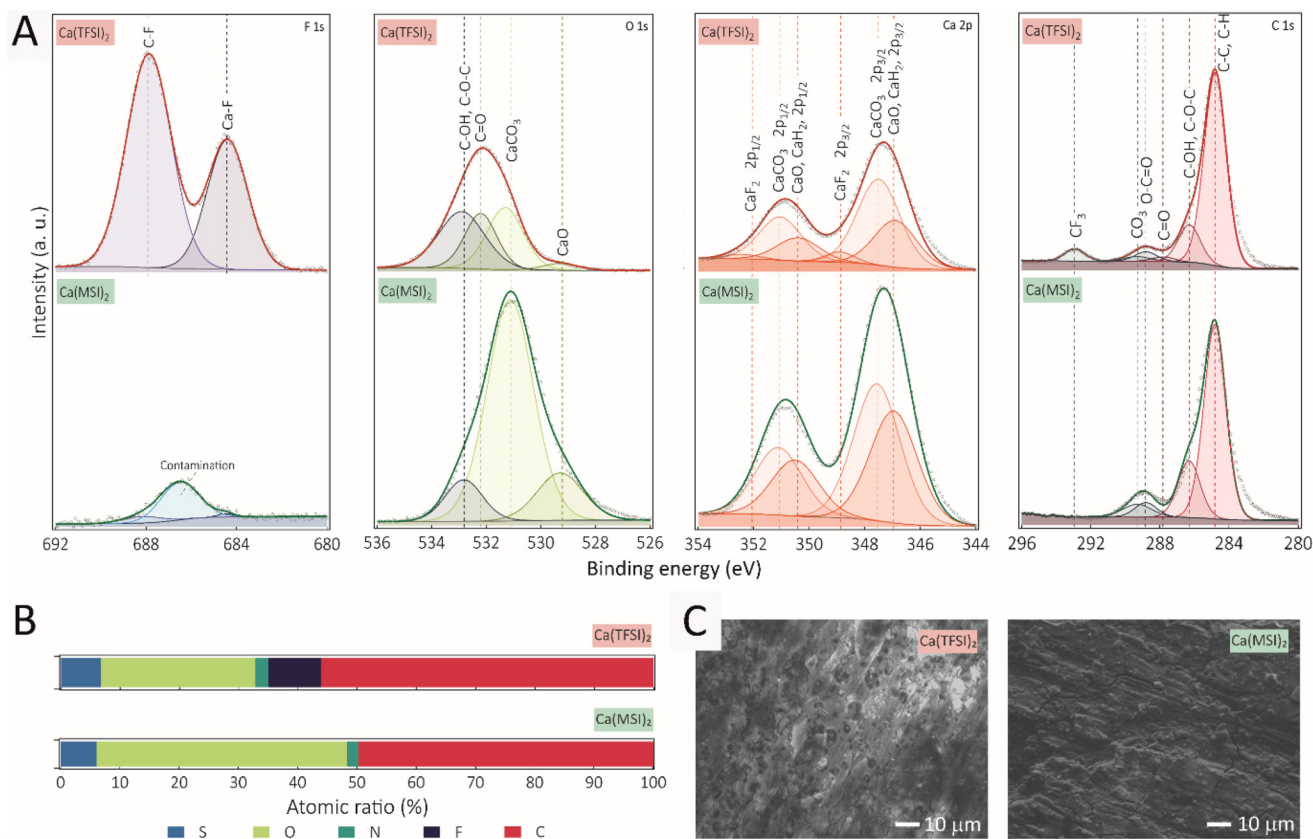
Fig. 4 (A) XPS profiles, (B) atomic ratio, and (C) SEM images of the SEIs formed on the Ca-electrode after 10 cycles in 0.5 M Ca(MSI)$_2$ and Ca(TFSI)$_2$ in DMAc electrolytes.

versus higher oxygen content for Ca(MSI)$_2$ – highlighting fundamentally different interfacial chemistries. Further plating experiments on Cu (Fig. S12 and S13) confirmed that Ca (TFSI)$_2$ forms a fluorine-rich, heavily decomposed SEI dominated by CaF$_2$, while Ca(MSI)$_2$ yields a fluorine-free, carbonate-rich, organic SEI. This chemical contrast directly affects performance: the resistive CaF$_2$ layer in Ca(TFSI)$_2$ hampers Ca^{2+} transport, leading to higher polarization, while the thinner, more uniform, CaF$_2$-free SEI in Ca(MSI)$_2$ facilitates improved ion transport and cycling stability. Morphological analysis (Fig. 4C) supports these conclusions – Ca(TFSI)$_2$ shows a rough, inhomogeneous surface; Ca(MSI)$_2$ yields a smoother Ca metal deposit, possibly the result of a more compact and homogeneous interphase favoring uniform electrodeposition.

Finally, to assess their practical applicability, the optimized electrolyte was tested in full Ca metal cells employing a 3,4,9,10-perylenetetracarboxylic dianhydride (PTCDA) organic cathode (Fig. S15). The cell delivered clear reversible charge–discharge profiles in 0.5 M Ca(MSI)$_2$ in DMAc, demonstrating efficient calcium plating and stripping at the metal anode and reversible redox activity of PTCDA,[41] while requiring further optimization for enabling efficient cycling of high voltage Ca-ion cathodes.[42] Although a gradual capacity fading was observed upon cycling, this degradation is attributed to the partial dissolution of PTCDA in the electrolyte. These results provide direct experimental evidence that the optimized electrolyte enables reversible Ca metal operation under realistic full-cell conditions, thereby validating its potential for integration into future calcium-based battery systems.

In summary, we introduce methanesulfonylimide (MSI$^-$), a fluorine-free anions that enables the design of high-performance and environmentally benign electrolytes for calcium metal batteries. Owing to its straightforward synthetic accessibility and absence of fluorinated moieties, the hydrogen-rich analogue of TFSI$^-$ offers a sustainable alternative to commercially available salts, whose degradation products often include corrosive and insulating fluorides. The Ca(MSI)$_2$/DMAc system exhibits stable and reversible Ca plating/stripping with lower overpotentials, and improved interfacial properties compared to its Ca(TFSI)$_2$-based counterpart. Spectroscopic and surface analyses reveal that the absence of fluorine prevents CaF$_2$ formation and instead promotes the growth of a uniform, organic-rich SEI that facilitates more efficient Ca^{2+} transport. This work highlights the importance of tuning solvation structures and interfacial chemistry through careful salt and solvent design. While a moderate increase in overpotential is observed during prolonged cycling, further enhancement of electrochemical stability and ionic conductivity is anticipated through future interfacial engineering strategies such as the integration of artificial SEI layers or

co-solvent optimization. Overall, this work contributes to a broader paradigm shift in SEI design for emerging rechargeable calcium metal batteries, offering valuable guidance for the development of safe, sustainable, and fluorine-free electrolytes.

Conflicts of interest

The authors declare no competing financial interest.

Data availability

Acknowledgements

References

1 J. Wang, J. Ma, Z. Zhuang, Z. Liang, K. Jia, G. Ji, G. Zhou and H. M. Cheng, *Am. Chem. Soc.*, 2024, **124**(5), 2839–2887, DOI: 10.1021/acs.chemrev.3c00884.

2 Y. Xu, Y. Du, H. Chen, J. Chen, T. Ding, D. Sun, D. H. Kim, Z. Lin and X. Zhou, *R. Soc. Chem.*, 2024, **53**, 7202–7298, DOI: 10.1039/d3cs00601h.

3 J. B. Goodenough and K. S. Park, *J. Am. Chem. Soc.*, 2013, **135**(4), 1167–1176, DOI: 10.1021/ja3091438.

4 B. Dunn, H. Kamath and J.-M. Tarascon, *Science*, 2011, **334**(6058), 928–935, DOI: 10.1126/science.1212741.

5 Q. Wei, L. Zhang, X. Sun and T. L. Liu, *R. Soc. Chem.*, 2022, **13**, 5797–5812, DOI: 10.1039/D2SC00267A.

6 I. D. Hosein, *ACS Energy Lett.*, 2021, **6**, 1560–1565, DOI: 10.1021/acsenergylett.1c00593.

7 J. D. Forero-Saboya, D. S. Tchitchekova, P. Johansson, M. R. Palacín and A. Ponrouch, *Adv. Mat. Interfaces*, 2022, **9**, 2101578, DOI: 10.1002/admi.202101578.

8 A. Ponrouch, C. Frontera, F. Bardé and M. R. Palacín, *Nat. Mater.*, 2016, **15**, 169–172, DOI: 10.1038/NMAT4462.

9 J. Forero-Saboya, C. Davoisne, R. Dedryvère, I. Yousef, P. Canepa and A. Ponrouch, *Energy Environ. Sci.*, 2020, **13**, 3423–3431, DOI: 10.1039/D0EE02347G.

10 C. Bodin, J. Forero-Saboya, P. Jankowski, K. Radan, D. Foix, C. Courrèges, I. Yousef, R. Dedryvère, C. Davoisne, M. Lozinšek and A. Ponrouch, *Batter. Supercaps*, 2023, **6**(1), e202200433, DOI: 10.1002/batt.202200433.

11 Z. Li, O. Fuhr, M. Fichtner and Z. Zhao-Karger, *Energy Environ. Sci.*, 2019, **12**, 3496–3501, DOI: 10.1039/C9EE01699F.

12 A. Shyamsunder, L. E. Blanc, A. Assoud and L. F. Nazar, *ACS Energy Lett.*, 2019, **4**, 2271–2276, DOI: 10.1021/acsenergylett.9b01550.

13 Z. Yang, N. J. Leon, C. Liao, B. J. Ingram and L. Trahey, *ACS Appl. Mater. Interfaces*, 2023, **15**, 25018–25028, DOI: 10.1021/acsami.3c01606.

14 A. M. Melemed, D. A. Skiba and B. M. Gallant, *J. Phys. Chem. C*, 2022, **126**, 892–902, DOI: 10.1021/acs.jpcc.1c09400.

15 T. Shinohara, K. Kisu, A. Dorai, K. Zushida, H. Yabu, S. Takagi and S. Orimo, *Adv. Sci.*, 2024, **11**(33), 2308318, DOI: 10.1002/advs.202308318.

16 D. Wang, X. Gao, Y. Chen, L. Jin, C. Kuss and P. G. Bruce, *Nat. Mater.*, 2018, **17**, 16–20, DOI: 10.1038/NMAT5036.

17 T. Mandai, H. Naya and H. Masu, *J. Phys. Chem. C*, 2023, **127**, 7987–7997, DOI: 10.1021/acs.jpcc.3c01160.

18 N. T. Hahn, D. M. Driscoll, Z. Yu, G. E. Sterbinsky, L. Cheng, M. Balasubramanian and K. R. Zavadil, *ACS Appl. Energy Mater.*, 2020, **3**, 8437–8447, DOI: 10.1021/acsaem.0c01070.

19 K. V. Nielson, J. Luo and T. L. Liu, *Batter. Supercaps*, 2020, **3**, 766–772, DOI: 10.1002/batt.202000005.

20 T. Pavčnik, J. D. Forero-Saboya, A. Ponrouch, A. Robba, R. Dominko and J. Bitenc, *J. Mater. Chem. A*, 2023, **11**, 14738–14747, DOI: 10.1039/D3TA02084C.

21 Z. Hou, R. Zhou, Y. Yao, Z. Min, Z. Lu, Y. Zhu, J. M. Tarascon and B. Zhang, *Angew. Chem., Int. Ed.*, 2022, **61**(50), e202214796, DOI: 10.1002/anie.202214796.

22 S. Yang, X. Wang, R. Li, Y. Zhou, H. Huang, M. Zhou, Y. Gao, W. Zhao, Y. Gao, Z. Pan and X. Yang, *Energy Environ. Sci.*, 2025, **18**, 1941–1951, DOI: 10.1039/D4EE04478A.

23 J. D. Forero-Saboya, E. Marchante, R. B. Araujo, D. Monti, P. Johansson and A. Ponrouch, *J. Phys. Chem. C*, 2019, **123**, 29524–29532, DOI: 10.1021/acs.jpcc.9b07308.

24 G. Asselin, Y. Wei, L. Gates, Y. Wang, J. L. Bao, W. Xu and N. Sa, *ACS Appl. Mater. Interfaces*, 2025, **17**, 13916–13927, DOI: 10.1021/acsami.4c20787.

25 X. He, J. Wang, Q. Cao, Y. Huang, H. Li, F. Tian, H. Song and C. Wang, *Adv. Sci.*, 2025, DOI: 10.1002/advs.202512339.

26 X. He, F. Tian, H. Song and C. Wang, *Chem. Eng. J.*, 2024, **502**, 157793, DOI: 10.1016/j.cej.2024.157793.

27 H. Zhang, U. Oteo, H. Zhu, X. Judez, M. Martinez-Ibañez, I. Aldalur, E. Sanchez-Diez, C. Li, J. Carrasco, M. Forsyth and M. Armand, *Angew. Chem., Int. Ed.*, 2019, **58**, 7829–7834, DOI: 10.1002/ange.201813700.

28 J. Foropoulos and D. D. Desmarteau, *Inorg. Chem.*, 1984, **23**(23), 3720–3723, DOI: 10.1021/ic00191a011.

29 J. D. Forero-Saboya, E. Marchante, R. B. Araujo, D. Monti, P. Johansson and A. Ponrouch, *J. Phys. Chem. C*, 2019, **123**, 29524–29532, DOI: 10.1021/acs.jpcc.9b07308.

30 H. Gudla, Y. Shao, S. Phunnarungsi, D. Brandell and C. Zhang, *J. Phys. Chem. Lett.*, 2021, **12**, 8460–8464, DOI: 10.1021/acs.jpclett.1c02474.

31 J. Self, N. T. Hahn, K. D. Fong, S. A. McClary, K. R. Zavadil and K. A. Persson, *J. Phys. Chem. Lett.*, 2020, **11**, 2046–2052, DOI: 10.1021/acs.jpclett.0c00334.

32 O. Borodin, G. D. Smith and W. Henderson, *J. Phys. Chem. B*, 2006, **110**, 16879–16886, DOI: 10.1021/jp061930t.

33 D. S. Tchitchekova, D. Monti, P. Johansson, F. Bardé, A. Randon-Vitanova, M. R. Palacín and A. Ponrouch, *J. Electrochem. Soc.*, 2017, **164**, A1384–A1392, DOI: 10.1149/2.0411707jes.

34 L. H. B. Nguyen and J. S. Filhol, *Adv. Energy Mater.*, 2023, **13**(27), 2300311, DOI: 10.1002/aenm.202300311.

35 H. Song, Y. Li, F. Tian and C. Wang, *Adv. Funct. Mater.*, 2022, **13**(21), 2200004, DOI: 10.1002/adfm.202200004.

36 S. A. McClary, D. M. Long, A. Sanz-Matias, P. G. Kotula, D. Prendergast, K. L. Jungjohann and K. R. Zavadil, *ACS Energy Lett.*, 2022, **7**, 2792–2800, DOI: 10.1021/acsenergylett.2c01443.

37 R. Sahore, A. Tornheim, C. Peebles, J. Garcia, F. Dogan, D. C. O'Hanlon, C. Liao, H. Iddir, Z. Zhang, J. Bareño and I. Bloom, *J. Mater. Chem. A*, 2017, **6**, 198–211, DOI: 10.1039/C7TA08289D.

38 B. W. Veal and A. P. Paulikas, *Phys. Rev. B*, 1985, **31**, 5399, DOI: 10.1103/PhysRevB.31.5399.

39 B. Demri and D. Muster, *Mater. Process. Technol*, 1995, **55**, 311–314, DOI: 10.1016/0924-0136(95)02023-3.

40 R. S. Lillard, D. G. Enos and J. R. Scully, *Corrosion*, 2000, **56**(11), 1119–1132, DOI: 10.5006/1.3294397.

41 O. Lužanin, A. K. Lautar, T. Pavčnik and J. Bitenc, *Mater. Adv.*, 2023, **5**, 642–651, DOI: 10.1039/D3MA00805C.

42 X. Guo, R. Markowski, A. Black, P. Apostol, D. Rambabu, O. Lužanin, T. Pavčnik, D. Monti, M. Du, D. Tie, X. Lin, V. Rao Bakuru, R. Delogne, K. Robeyns, L. Simonelli, J.-F. Gohy, J. Bitenc, J. Wang, A. Ponrouch and A. Vlad, *Energy Environ. Sci.*, 2025, **18**, 9114–9124, DOI: 10.1039/d5ee02567b.